

Failure in laboratory fault models in triaxial tests

J. C. Savage, D. A. Lockner, and J. D. Byerlee

U.S. Geological Survey, Menlo Park, California

Abstract. A model of a fault in the Earth is a sand-filled saw cut in a granite cylinder subjected to a triaxial test. The saw cut is inclined at an angle α to the cylinder axis, and the sand filling is intended to represent gouge. The triaxial test subjects the granite cylinder to a constant confining pressure and increasing axial stress to maintain a constant rate of shortening of the cylinder. The required axial stress increases at a decreasing rate to a maximum, beyond which a roughly constant axial stress is sufficient to maintain the constant rate of shortening. Such triaxial tests were run for saw cuts inclined at angles α of 20°, 25°, 30°, 35°, 40°, 45°, and 50° to the cylinder axis, and the apparent coefficient of friction μ_a (ratio of the shear stress to the normal stress, both stresses resolved onto the saw cut) at failure was determined. Subject to the assumption that the observed failure involves slip on Coulomb shears (orientation unspecified), the orientation of the principal compression axis within the gouge can be calculated as a function of μ_a for a given value of the coefficient of internal friction μ_i . The rotation of the principal stress axes within the gouge in a triaxial test can then be followed as the shear strain across the gouge layer increases. For $\mu_i \sim 0.8$, an appropriate value for highly sheared sand, the observed values μ_a imply that the principal axis of compression within the gouge rotates so as to approach being parallel to the cylinder axis for all saw cut angles ($20^\circ < \alpha < 50^\circ$). In the limiting state (principal compression axis parallel to cylinder axis) the stress state in the gouge layer would be the same as that in the granite cylinder, and the failure criterion would be independent of the saw cut angle.

Introduction

This paper is concerned with the stress state in the gouge layer within a fault at the time of failure. The importance of this problem in fault mechanics was explained by *Rice* [1992], who showed that plastic deformation of the relatively weak gouge may cause a stress field to develop in the gouge layer that is distinct from the stress field outside the fault zone. For example, this difference in stress fields might permit pore pressures to develop within the fault zone in excess of those that would cause hydrofracture outside the zone. This potential for high pore pressure within the fault zone would explain how the San Andreas fault could undergo strike slip even though the principal compression axis outside the fault zone makes a steep angle with the fault zone itself. Unfortunately, a direct calculation of the stress field within the gouge layer is not possible, because there is no generally agreed upon theory of Coulomb plasticity, the flow of granular materials [*Rice*,

1992, p. 484]. However, the stress field that develops within the gouge as the fault is loaded can be measured experimentally.

Mandl [1988, p. 314] has already measured the stress field within a gouge layer in the particular case in which the fault zone is loaded by a constant normal stress and an increasing shear stress. He found in that case that the axis of principal compression within the gouge layer rotated to a 45° inclination to the fault plane as the shear stress was increased. Thus, whatever the stress state in the fault blocks on either side of the fault, the stress at failure in the gouge approaches a state that can be described as the sum of a hydrostatic stress and a shear stress parallel to the fault. *Byerlee and Savage* [1992] explained how Coulomb plasticity in the gouge layer might produce that rotation, but in doing so invoked Saint Venant's hypothesis (principal strain rate axes parallel to the principal stress axes), a hypothesis that is probably not valid for the flow of granular materials [*Mandl*, 1988, p. 312]. (The arguments of *Byerlee and Savage* had been published earlier and in greater detail by *Hansen* [1961].) Nevertheless, *Mandl's* experiment does provide an empirical solution for the reorientation of the stress field within the gouge under the particular loading conditions employed. Here we describe experiments that provide empirical solutions for

This paper is not subject to U.S. copyright. Published in 1996 by the American Geophysical Union.

Paper number 96JB02094.

the stress state in the gouge layer under other loading conditions.

The stress state in gouge-filled faults can be studied by observing the failure of simple model faults in the laboratory [Byerlee *et al.*, 1978; Logan *et al.*, 1979]. The models consist of granite cylinders cut through by a saw cut inclined at an angle α to the cylinder axis (Figure 1). The saw cut is filled with a synthetic gouge (in this case Ottawa sand), and the cylinder is subjected to a triaxial test to failure (slip on the saw cut). In a triaxial test the cylinder is confined by a constant lateral pressure P_c , and the axial compression σ'_1 (Figure 1) is increased so as to maintain a constant rate of shortening of the cylinder. The principal stresses in the granite cylinders are a compression σ'_1 along the cylinder axis and the lateral compression $\sigma'_2 = P_c$ perpendicular to the axis. (The prime identifies stresses within the granite cylinder.) The shear stress τ and normal stress σ across the saw cut are

$$\begin{aligned}\tau &= 0.5 (\sigma'_1 - P_c) \sin 2\alpha \\ \sigma &= 0.5 (\sigma'_1 + P_c) - 0.5 (\sigma'_1 - P_c) \cos 2\alpha\end{aligned}\quad (1)$$

(The absence of a prime denotes that those stresses obtain within the gouge layer. Of course, in this case, continuity of stress across the boundary requires that the same stresses obtain within the granite cylinder.)

Data

Experiment

Fault models of the form shown in Figure 1 were prepared for seven different angles, $\alpha = 20^\circ, 25^\circ, 30^\circ, 35^\circ, 40^\circ, 45^\circ,$ and 50° . The synthetic gouge was Ottawa sand with an initial grain diameter of about 0.2 mm and initial gouge layer thickness of 2 mm. The independent

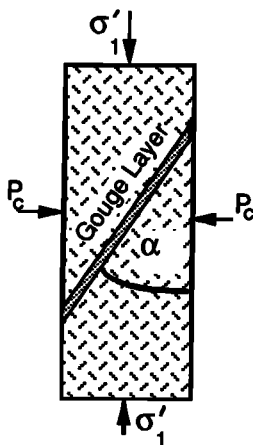


Figure 1. Fault model subjected to triaxial test. The gouge is a layer of sand in a saw cut through the granite cylinder.

variable in a triaxial test is the axial shortening of the cylinder. That shortening is due to elastic compression of the granite cylinder and gouge layer, compaction of the gouge, and intense shear within the gouge layer (i.e., apparent slip on the saw cut). We have corrected for the elastic compression. The remaining axial shortening δz is attributed to a nominal shear strain $\delta z / (d \cos \alpha)$ across the saw cut, where d is the initial gouge thickness. The imposed axial shortening rate is roughly equivalent to a nominal shear strain rate of $10^{-3}/s$. The axial stress σ'_1 (measured by an external load cell) is plotted in Figure 2 as a function of this nominal shear strain for specimens with different saw cut angles. In seven of the tests (one for each saw cut angle) the confining pressure P_c (Table 1) was chosen so that failure (slip on the saw cut) occurred at about the same (750 ± 100 MPa) normal stress across the saw cut. Two additional tests, one on a 30° and the other on a 45° saw cut, were run at a somewhat lower (500 MPa) normal stress.

Three quantities (axial force, P_c , and δz) are measured at a sampling rate of 1/s during each test. Confining pressure P_c is measured with a manganin cell calibrated against a precision pressure gage. The estimated accuracy (2 standard deviations) in measuring P_c is ± 0.4 MPa, and the precision (repeatability) is about ± 0.3 MPa (2 standard deviations). The measured axial force used to calculate σ'_1 has been corrected for seal friction, and the measurement accuracy is estimated to be $\pm 0.3\%$. The axial displacement δz is measured with a DCDT displacement transducer with a linearity of $\pm 0.5\%$. Thus the primary measurements are of relatively high accuracy.

Problems in accuracy arise primarily in inferring σ'_1 from the measured axial force and axial displacement. The problem is associated with the sliding of the upper granite cylinder with respect to the lower granite cylinder (Figure 1). That slip causes the contact area between the two cylinders to decrease and thus causes the axial stress to be underestimated. The axial stress is corrected for this geometric effect as described by Scott *et al.* [1994a, p. 774]; all axial stresses reported in this paper include that correction. To maintain alignment, slip of the upper half cylinder over the lower half cylinder on the saw cut must be associated with slip of the lower half cylinder to the right relative to the piston forcing it from below (Figure 1). We facilitate that slip by including a 0.13-mm-thick shim of greased Teflon between the lower half granite cylinder and the piston. Although accuracy in measuring σ'_1 almost certainly decreases as the nominal shear strain increases, we believe our procedures are adequate for slip displacements on the model fault up to about 10 mm (nominal shear strain about 5). Measurements beyond nominal shear strain 5 were not attempted. At a shear strain of 4, the accuracy (2 standard deviations) in estimating σ'_1 is approximately $\pm 1\%$, and repeatability (2 standard deviations) between experiments (different specimens) is about 4%. Error bars in Figures 3 and 4 are based on the latter estimate of uncertainty. Repeatability

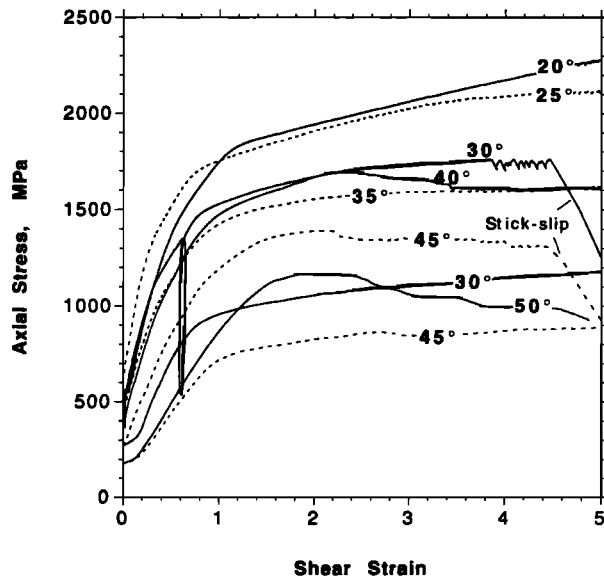


Figure 2. Axial stress as a function of the shear strain across the saw cut for triaxial tests of saw cuts at angles of 20°, 25°, 30°, 35°, 40°, 45°, and 50° with cylinder axis.

bility (2 standard deviations) in measuring the ratio of the shear to normal stresses across the saw cut at failure $\tau_f/\sigma_f = \mu_a$ is estimated to be about ± 0.03 , the value used for the error bars in Figure 6.

In Figure 2 the axial stress σ'_1 initially increases at a decreasing rate and eventually attains a maximum; it may then decrease slightly from that maximum at greater strain. Except for the 20° and low-stress 30° (lower of the two 30° curves) data in Figure 2, that limiting stress level is attained by the time the nominal shear strain is equal to 4, and we have taken the stresses at that shear strain to represent the failure asymptote.

We admit that this is not a precise choice, and we will later (Figure 7) give a complete treatment of all of the data, not just the data at maximum stress. The values of σ'_1 and P_c at shear strain 4 are shown in Table 1 for the various saw cut angles. Also shown in the table are the shear τ_f and normal σ_f stresses across the saw cut at failure as calculated from (1).

The axial stress σ'_1 for failure at shear strain 4 is plotted as a function of confining pressure P_c in Figure 3a for the seven saw cut angles. Also shown (dashed line) is the axial stress at failure for an intact granite cylinder (quadratic fit to data from *Byerlee* [1966, Table 7]). Although it is not discussed further in this paper, a 15° saw cut was also tested in the triaxial apparatus at a confining pressure of 500 MPa. In this case the saw cut remained intact, and the granite cylinder itself failed at $\sigma'_1 = 2292$ MPa (open circle in Figure 3a). Failure of the 15° saw cut at $P_c = 500$ MPa apparently would occur at some axial stress $\sigma'_1 > 2292$ MPa. The strength of the 15° saw cut should have been measured at a lower confining pressure.

In Figure 3b we have plotted other data from three similar experiments. (1) The low-stress data shown by pluses (G&W30°) in Figure 3b are from *Gu and Wong* [1994, Table 1, samples GU22, 4, 5, 1, 10, 13, 12, and 11] for ultrafine (particle size of ~ 0.006 mm) sand in a 30° saw cut. (2) Also shown are data from *Summers and Byerlee* [1977, pp. 45–77] for Ottawa sand (particle size of ~ 0.2 mm) in 30° (S&B30°) and 45° (S&B45°) saw cuts (crosses in Figure 3b). (Only stress measurements from *Summers and Byerlee* [1977] made after at least 5 mm of cumulative slip on the saw cut are shown in Figure 3b. Those stresses were corrected for the change in contact area imposed by that slip [*Scott et al.*, 1994a, p. 774]. The *Summers and Byerlee* data at $P_c = 470$ MPa involve stick-slip events with large stress drops. Those stress drops may have disturbed the

Table 1. Stresses at Failure at Shear strain 4 for Various Saw Cut Angles α

α , deg	Granite		Gouge			$\xi(\mu_i = 0.8)$, deg
	P_c , MPa	σ'_1 , MPa	σ_f , MPa	τ_f , MPa	τ_f/σ_f	
20	500.0	2168.0	695.1	536.1	0.771	32.28 (20.08 ^a)
25	485.0	2084.9	771.2	613.3	0.795	28.26
30	270.1	1142.7	488.2	377.9	0.774	31.89
30	420.4	1719.6	745.2	562.5	0.755	34.12
35	375.3	1593.5	776.4	573.3	0.738	35.83
40	350.2	1612.4	871.6	621.5	0.713	38.09
45	175.2	869.8	522.5	347.3	0.665	41.98
45	270.1	1326.5	799.9	529.6	0.662	42.20
50	174.9	992.5	654.5	402.5	0.615	45.71

^aValue in parentheses corresponds to solution for the lower branch of the two-valued function given by (2).

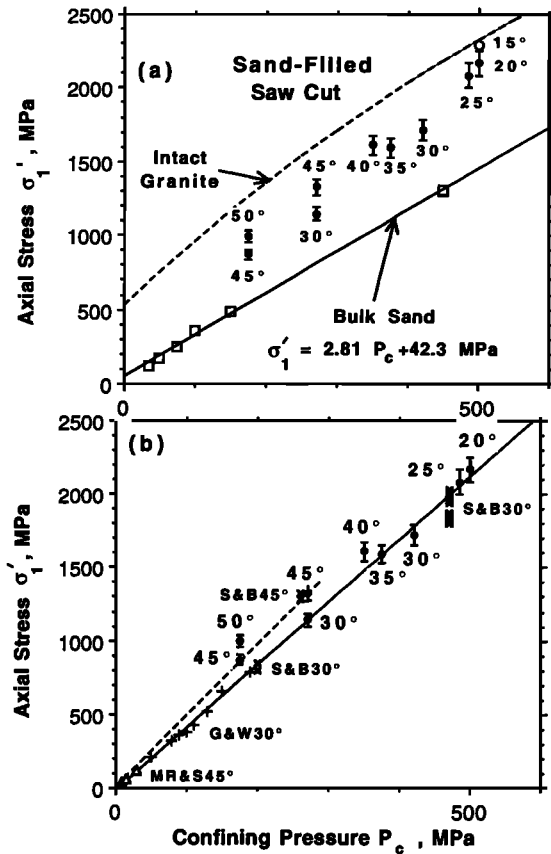


Figure 3. Plots of the limiting axial stress at failure as a function of confining pressure for saw cuts at various angles (solid circles). Error bars represent 2 standard deviations on either side of the plotted point. (a) Failure stresses for triaxial tests of intact granite and bulk sand as well as saw cut data from this paper. The open circle represents a failed attempt to measure the strength of a 15° saw cut. (b) Additional failure data for 30° and 45° saw cuts from *Summers and Byerlee* [1977] (crosses), *Gu and Wong* [1994] (pluses), and *Marone et al.* [1990] (open triangles). The solid line is a fit to the G&W30° saw cut data, and the dashed line is a fit to the 45° saw cut data.

compaction of the sand layer. This disturbance would account for the scatter in the measured strengths. If so, the largest values of σ'_1 would be the preferred measure of strength.) (3) Finally, data (open triangles labeled MR&S45°) from *Marone et al.* [1990] for ultrafine sand in a 45° saw cut at low stresses are plotted in Figure 3b. Notice that linear extrapolation of the Gu and Wong 30° saw cut data (solid line in Figure 3b) predicts reasonably well both the 30° saw cut data (S&B30°) from Summers and Byerlee and our own two 30° saw cut measurements (solid circles). Moreover, the 45° saw cut data (MR&S45°, S&B45°, and our own two 45° measurements) also appear to be colinear (dashed line in Figure 3b). Both of these linear representations have near-zero intercepts, which suggest negligible cohesion. On this basis we suggest that the zero intercept line passing through a datum (solid circle) for a particular saw cut angle represents the locus for the axial stress

at failure on saw cuts of that angle for any confining pressure.

The same data as shown in Figure 3b are replotted in Figure 4a in terms of shear and normal stresses resolved across the saw cut. In that figure we have drawn lines from the origin through our two 30° saw cut data points (solid line) and through our two 45° saw cut data points (dashed line). The other 30° saw cut data (Gu and Wong and Summers and Byerlee) and 45° saw cut data (Marone et al. and Summers and Byerlee) are reasonably consistent with these linear representations of the 30° and 45° saw cut strengths. A linear fit to all of the data for a particular saw cut angle, of course, would furnish a better representation. The point here, however, is that even with a strength measurement at just one normal stress one can define an approximate strength locus for all normal stresses for a particular saw cut angle. We propose that the saw cut strength for a particular saw cut angle is approximated in the $\sigma - \tau$ plane by the straight line with zero intercept passing through a single measured strength datum for that saw cut. On that basis, saw cut strengths for saw cut an-

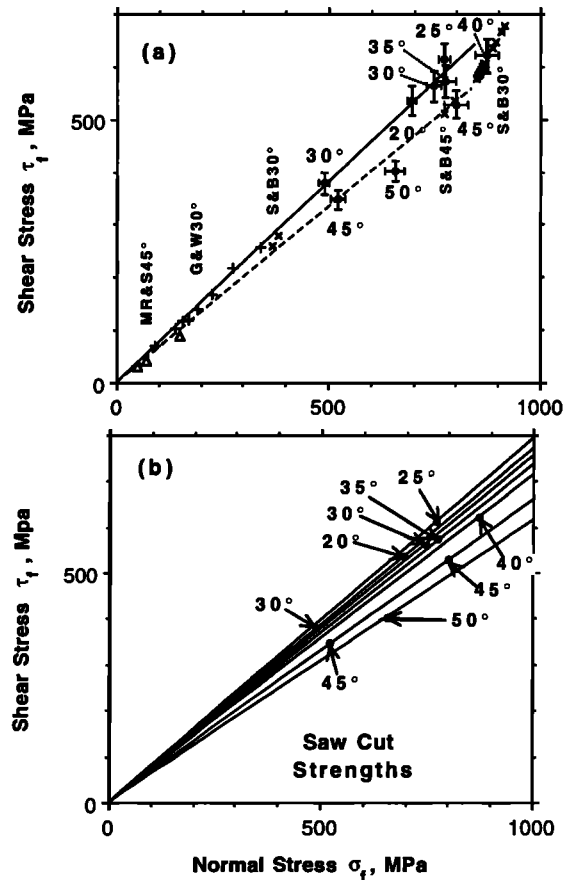


Figure 4. Plots of the saw cut failure data in the limiting state in terms of the shear and normal stresses resolved across the saw cuts. Error bars represent 2 standard deviations on either side of the plotted point. (a) Data from Figure 3b. (b) Saw cut strengths at various saw cut angles inferred from a single failure datum for each angle and an assumed zero cohesion.

gles of 20°, 25°, 30°, 35°, 40°, 45°, and 50° are shown in Figure 4b.

Figure 4b summarizes the observations on the strength of strain-hardened, sand-filled saw cuts. The strength curve for each saw cut angle has been represented by a straight line with zero intercept that passes through the single high-normal-stress strength datum that we have observed for that particular saw cut angle. The actual saw cut strengths may have small intercepts and even some curvature, but the observations available are not adequate to determine those parameters. To the extent that the straight lines in Figure 4b represent the saw cut strengths, only one parameter is required to characterize the saw cut strength for a particular saw cut angle, the slope of the strength line. That slope, $\mu_a = \tau_f/\sigma_f$, is the apparent friction on the saw cut. The observed values of μ_a at shear strain 4 are tabulated in Table 1.

A cursory examination of the structural fabric of the gouge layers in the unloaded specimens showed a well-resolved set of shears that on the basis of their orientation are identified as R_1 shears. Those shears were inclined at about $15^\circ \pm 5^\circ$ to the plane of the saw cut regardless of the saw cut angle. In addition, shear zones within the gouge but along the gouge-granite boundary were observed. No distinctive differences in the fabric that could be correlated with saw cut angle were noted. *Byerlee et al.* [1978] had previously noted that there were no distinctive differences observed between the fabrics of gouge layers in 30° and 45° saw cuts.

Coefficient of Internal Friction

In the subsequent discussion we will need the coefficient of internal friction μ_i of the highly sheared sand within the saw cuts. Although μ_i for compacted sand has been measured directly (see below), the value of μ_i for highly sheared sand has only been inferred. *Scott et al.* [1994b] estimate from the maximum observed value of μ_a (the apparent coefficient of friction) measured in a double-direct-shear apparatus that $\mu_i = 0.85 \pm 0.04$ (value quoted by *Scott et al.* [1994a, p. 768]) for highly sheared Ottawa sand. The maximum observed μ_a was taken to be $\sin \phi$, from which $\mu_i = \tan \phi$ was inferred. *Gu and Wong* [1994] inferred $\mu_i = 0.80$ for highly sheared sand from the observed orientation of Coulomb shears within a 30° saw cut.

A direct measurement of μ_i for compacted (but not highly sheared) sand is $\mu_i = 0.54$. That value is based on triaxial tests of cylinders made wholly of compacted sand. The axial stress at failure for these cylinders is shown as a function of confining pressure P_c in Figure 3a (open squares). The data for $P_c \leq 150$ MPa were taken from *Zoback and Byerlee* [1976, Figure 8], and the single measurement at $P_c = 450$ MPa was made more recently (D. A. Lockner, unpublished data, 1995). A straight line of slope 2.814 ± 0.072 and intercept 42.3 MPa furnishes a good fit to those data (bulk sand in Figure 3a). The corresponding failure envelope in the $\sigma - \tau$ plane [*Jaeger and Cook*, 1971, p. 90] is a straight line with slope $\mu_i = 0.540 \pm 0.015$ and intercept $S_0 = 12.6$ MPa. That is, the measured coefficient of internal friction of

compacted (but not highly sheared) sand is $\mu_i = 0.54$. That value is obviously not representative of the highly sheared sand in the saw cuts in our experiments, as the apparent coefficients of friction τ_f/σ_f across the saw cuts are all larger than 0.54 (Table 1). That μ_i should be larger for the highly sheared sand in the saw cuts than for the compacted sand is an expected consequence of the strain hardening evident in Figure 2. That strain hardening is associated with shear-induced compaction of the gouge [*Marone et al.*, 1990], most of which occurs at shear strains less than about 1.

Rotation of Principal Stress Axes

In the previous section we have been concerned with the limiting state in which steady shearing occurs at a constant coefficient of apparent friction. We now explain how that limiting state is attained. We follow the procedures outlined by *Gu and Wong* [1994] to find the stress state within the sand layer subject only to the assumption that shearing across the saw cut is accommodated by Coulomb plasticity (i.e., distributed, cooperative slip on two sets of Coulomb shears [*Jaeger and Cook*, 1971, pp. 393–399]). The Mohr circle that represents the stress state in the gouge layer at failure must then be tangent to the Coulomb failure envelope (Figure 5a), which we take to be a straight line of slope μ_i and zero intercept (i.e., we treat gouge as cohesionless). The other condition upon the Mohr circle is that it must pass through the point (σ_f, τ_f) (Table 1) that describes the stresses observed across a plane parallel to the saw cut at failure. As shown in the appendix, those two conditions define two Mohr circles, one of which must represent the stress state within the gouge layer at failure. Given the Mohr circle describing the stress state, one can solve (see appendix) for the angle between the principal axis of compression and the plane of the saw cut:

$$\xi = \pi/2 - 0.5 \tan^{-1} \left\{ (\tau_f/\sigma_f) / \left[-\mu_i^2 \pm ((\mu_i^2 + 1) (\mu_i^2 - \tau_f^2/\sigma_f^2))^{1/2} \right] \right\}, \quad (2)$$

a relation given earlier in slightly different form by *Gu and Wong* [1994, equation (3)]. The value of ξ is plotted as a function of $\mu_a = \tau_f/\sigma_f$ in Figure 6a for various values of μ_i . Also shown in Figure 6a is the saw cut angle α plotted as a function of the value of the ratio τ_f/σ_f observed on the saw cut of that angle at shear strain 4 (Table 1). The plotted values of α fall roughly along the contour $\mu_i = 0.8$. We argued in the previous section that $\mu_i = 0.8$ is, in fact, a good estimate of the coefficient of internal friction for extensively sheared Ottawa sand. The values of ξ predicted from (2) for values of μ_a at shear strain 4 for $\mu_i = 0.8$ are shown in Table 1. The near equality of the inferred ξ for a given saw cut angle and the saw cut angle itself implies that the axis of principal compression within the gouge is nearly aligned with the axis of the granite cylinder

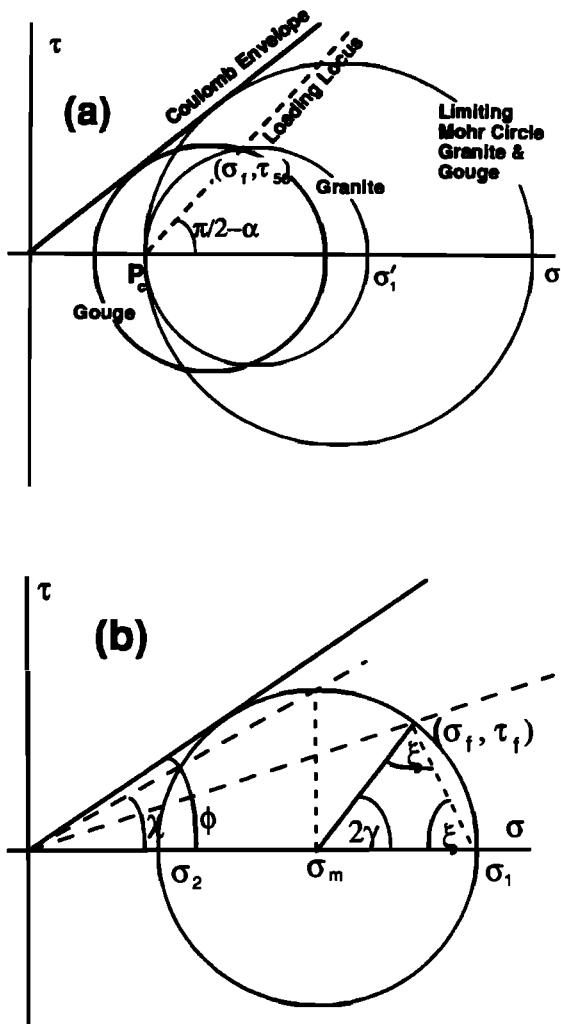


Figure 5. (a) Mohr circles representing the stress state in the granite cylinder (smallest circle) and gouge layer (intermediate circle). The largest circle represents the limit approached by the other two circles as σ'_1 increases. (b) Mohr circle for stress in the sand layer within the saw cut at failure. Here, $\sigma_m = (\sigma_1 + \sigma_2)/2$ and τ_f and σ_f are the shear and normal stress across the saw cut at failure. The heavy diagonal line represents the Coulomb failure criterion, zero cohesion assumed.

at shear strain 4. The angular difference $\xi - \alpha$ between these two axes is shown in Figure 6b as a function of the saw cut angle.

To the extent that Coulomb plasticity accommodates deformation in the sand layer, the variation of σ'_1 as a function of shear strain in Figure 2 can be explained by stress changes in the sand layer that involve rotation of the principal stress axes. This explanation, of course, assumes that μ_i remains constant, an assumption that is probably valid once the maximum density of the sand has been attained (i.e., at shear strains greater than about 1). Figure 2 defines σ'_1 at a particular confining pressure P_c (Table 1) as a function of shear strain on each saw cut. Then τ_f , σ_f , and the ratio $\mu_a = \tau_f/\sigma_f$ can be calculated as functions of shear strain from (1).

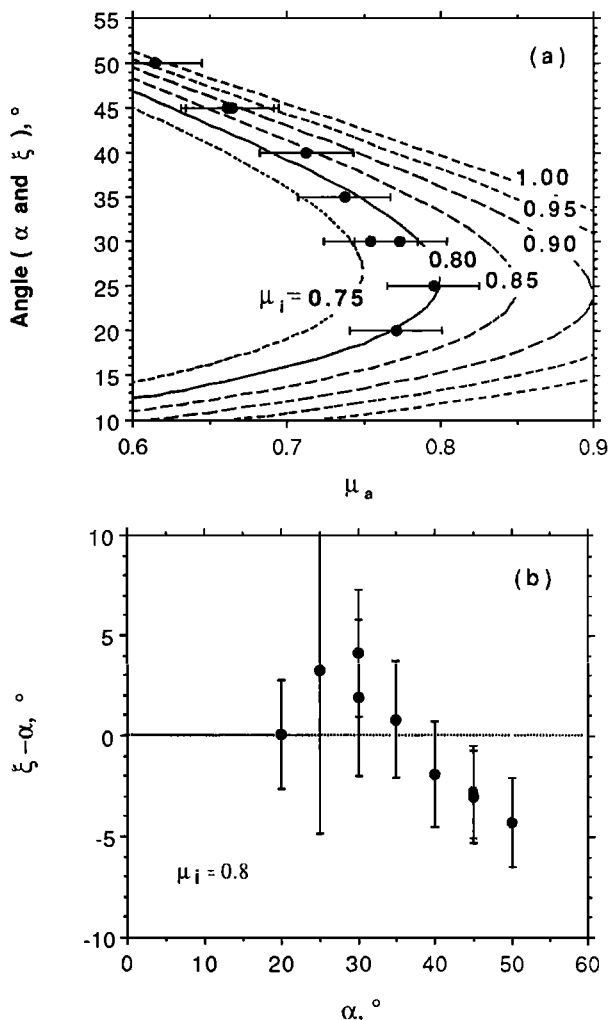


Figure 6. (a) The angle ξ (lines) between the principal compression axis in the sand layer and the plane of the saw cut plotted as a function of the apparent friction on the saw cut $\mu_a = \tau_f/\sigma_f$ for various values of the coefficient of internal friction. Also plotted (solid circles) is the saw cut angle α as a function of μ_a measured at shear strain 4 (Table 1). (b) Inclination of principal axis of compression in the sand layer with respect to the cylinder axis as a function of saw cut angle. Error bars represent 2 standard deviations on either side of the plotted point.

The values of μ_a calculated in this way are shown in Figure 7a. Then ξ , the angle between the principal axis of compression and the plane of saw cut, may be calculated from (2). The values of ξ calculated for $\mu_i = 0.807$ and $\mu_i = 0.85$ are shown in Figures 7b and 7c. In that calculation we have chosen the + sign in the \pm option in (2). That choice corresponds to the upper limbs of the curves plotted in Figure 6a and, as will be discussed later, provides continuity with the elastic solution at shear strains < 1 [Gu and Wong, 1994, pp. 414-416]. As can be seen in Figure 7, ξ generally decreases with increasing shear strain, approaching an asymptote close to the saw cut angle itself ($\xi \rightarrow \alpha$). The 20° saw cut does not approach such an asymptote within the range of shear strains shown in Figure 7. The effect of in-

creasing μ_i (compare Figures 7b and 7c) is to increase ξ by an amount that decreases as the saw cut angle increases.

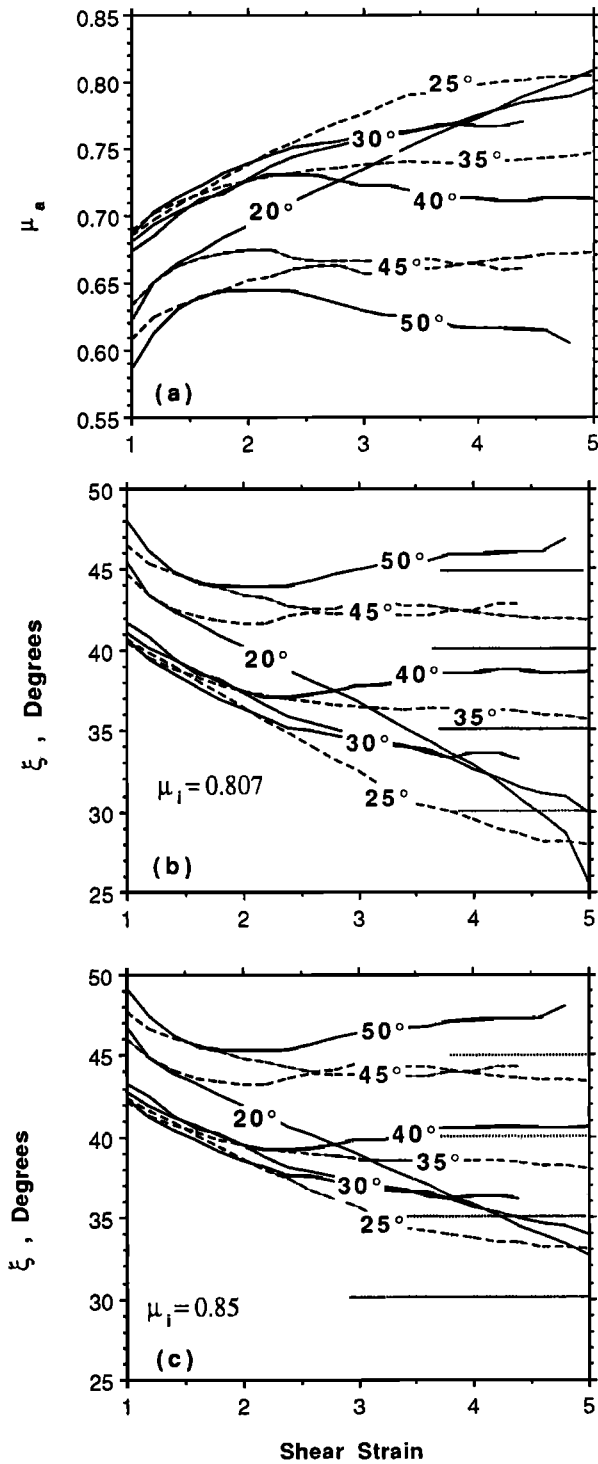


Figure 7. (a) Apparent coefficient of friction on saw cuts as a function of shear strain as calculated from the data of Figure 2. (b) Inclination of the principal compression axis in the sand with respect to the saw cut as a function of shear strain for an assumed coefficient of internal friction $\mu_i = 0.807$. (c) Same as Figure 7b but for $\mu_i = 0.85$.

Figures 7b and 7c suggest that the axis of principal compression rotates into approximate coincidence with the cylinder axis ($\xi \rightarrow \alpha$). This is shown more clearly in Figure 8, in which the difference $\xi - \alpha$ is plotted as a function of shear strain. The asymptotic convergence $\xi - \alpha \rightarrow 0$ is particularly clear in Figure 8a ($\mu_i = 0.807$) but is still apparent in Figure 8b ($\mu_i = 0.85$).

Discussion

The initial response of the gouge to the loading in a triaxial test is, of course, elastic, but the subsequent response involves flow of the gouge, which is properly described as plastic. *Gu and Wong* [1994, pp. 414-416] discussed the elastic solution for a gouge layer in a saw cut and concluded that the principal compression axis would be inclined to the plane of the saw cut at an angle greater than 45° . A stage of inelastic compaction of the sand layer follows the elastic stage [*Marone et al.*, 1990], but we are unable to follow the rotation of the principal compression axis in that stage. Beyond a shear strain of about 1, deformation appears to be accommodated by Coulomb plasticity and involves a rotation of the prin-

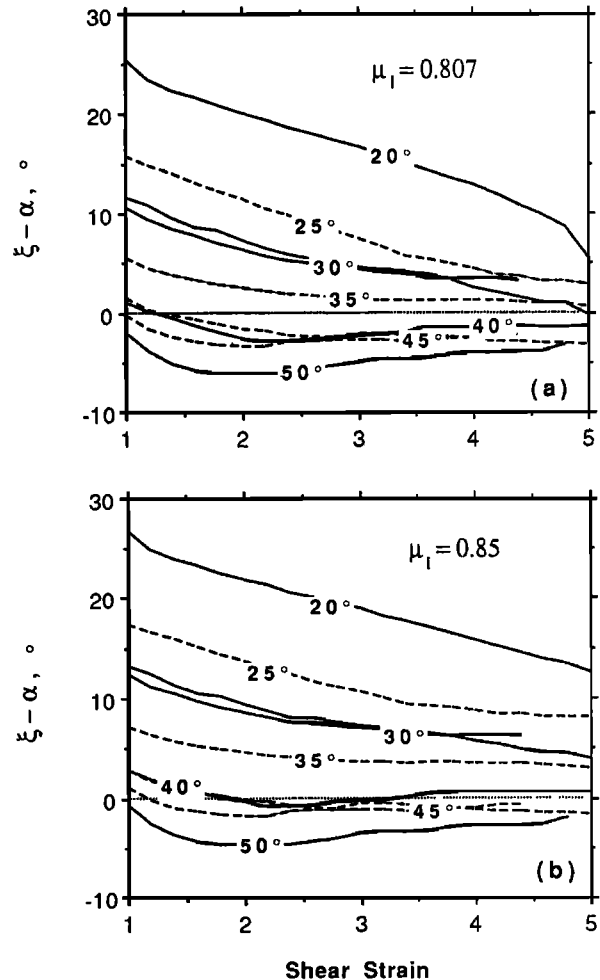


Figure 8. (a) Inclination of the axis of greatest compression with respect to the cylinder axis for $\mu_i = 0.8$. (b) Same as Figure 8a except $\mu_i = 0.85$.

principal stress axes within the gouge layer. The rotation comes about as follows [Rice, 1992, p. 481]: Stress continuity requires that the shear and normal stress across the saw cut be given by equation (1). However, the compression parallel to the saw cut is determined by the plastic solution, and as that stress changes in response to flow, the principal stress axes rotate. We have followed the rotation of the principal compression axis beyond shear strain 1 (Figures 7b and 7c). Notice that the orientation of the principal compression axis with respect to the plane of the saw cut is about 45° at shear strain 1 (Figures 7b and 7c), roughly consistent with the orientation ($>45^\circ$) predicted from elastic theory at much lower shear strains. Had we used the alternative solution for ξ in equation (2) (the $-$ sign in the \pm option), the inclination of the principal compression axis to the plane of the saw cut would have been about 15° at shear strain 1. This is the justification for choosing the $+$ sign in the \pm option in equation (2) in constructing Figures 7 and 8.

The solution for the stress state in the gouge layer at shear strains >1 is summarized in Figure 5a. The Mohr circle for the stress state in the granite cylinder is specified by the principal stresses σ'_1 and P_c (Figure 5a). After the initial hydrostatic loading in the triaxial test, the loading trajectory for the saw cut is $\tau = (\sigma - P_c) \tan \alpha$ (eliminate σ'_1 from equations (1)), which is shown by the dashed line in Figure 5a. The intersection of that dashed line with the Mohr circle for the granite cylinder defines the shear and normal stresses (τ and σ) across the saw cut at axial stress σ'_1 . Beyond a shear strain of about one the Mohr circle for the stress state within the gouge is then the circle passing through (σ_f, τ_f) , which is tangent to the Coulomb failure envelope (Figure 5a). In the triaxial test, P_c is held constant, but σ'_1 must generally be increased (Figure 2) to maintain a constant rate of shortening of the cylinder. As σ'_1 increases, the Mohr circle for the granite cylinder expands by moving its center to the right with the left-hand edge of the circle held at P_c (Figure 5a). This expansion causes a corresponding increase in both σ_f and τ_f (intersection of Mohr circle with the loading locus) and a consequent growth of the Mohr circle representing the stress state in the gouge. The limiting stress state occurs when the Mohr circle for the granite cylinder becomes tangent to the Coulomb failure envelope for the gouge. At that state the Mohr circles for the gouge and granite cylinder coincide.

The decrease in axial stress for saw cut angles of 40° , 45° (upper of two curves), and 50° shown in Figure 2 for shear strains >2 may be in part an experimental artifact. Those specimens showed some cracking of the granite near the cylindrical surface at the top and bottom of the saw cut. That damage could have decreased the effective contact area, which would cause us to underestimate the effective axial stress. However, because the curves for μ_a and ξ are relatively flat beyond shear strain 2 (Figures 7 and 8) for the 40° , 45° , and 50° saw cuts, it makes little difference whether stresses are measured at shear strain 4 or at the maximum of σ'_1 in Figure 2 (i.e., near shear strain 2).

The orientation of the stress field within the sand layer in triaxial experiments is distinctly different from that found in shear-box-type experiments (e.g., shear box, double-direct-shear, and rotary shear apparatus) in which shear loading is applied across the sand layer at constant normal stress. In shear-box-type experiments the principal compression axis in the sand layer is found to rotate to a 45° inclination with the plane of the layer [Mandl, 1988, p. 314; Scott et al., 1994b]. In the triaxial experiments we have found that the principal compression axis rotates toward the axis of the cylinder ($\xi \rightarrow \alpha$ in Figure 7b). For the 45° and 50° saw cuts that rotation causes the principal compression axis to be inclined at about 45° to the saw cut, an inclination no different from that found in the shear-box-type experiments. However, for the other saw cut angles the inclination is distinctly different from 45° . A generalization that is consistent with both types of experiments (shear-box and triaxial) is that the principal compression axis tends to rotate into coincidence with the principal compression axis of the incremental loading. In the shear-box-type experiments the incremental load, a shear stress across the sand layer, involves principal compression inclined at 45° to the layer, consistent with the limiting orientation of the principal compression axis in the sand layer. In the triaxial experiments the incremental loading, axial compression, involves principal compression along the cylinder axis, consistent with the observed limiting orientation of the principal compression axis with the sand layer.

To the extent that the principal compression axis in the gouge layer rotates into coincidence with the cylinder axis, the stress state in the gouge is identical with that in the granite cylinder (see appendix). The stress state in the gouge is then the same as if the entire cylinder were composed of gouge. If the mechanism of failure involves Coulomb plasticity, then the failure criterion would be independent of the saw cut angle. Specifically, in a plot of σ'_1 versus P_c , all of the failure data should lie along a straight line with near-zero intercept. Reference to Figure 3b shows that failure data are roughly consistent with a linear failure criterion. A better fit should not be expected, because the principal compression axes at shear strain = 4 are not exactly parallel to the cylinder axis (Figure 8).

It is generally assumed that the orientation of the R_1 shears (slip lines in the velocity field) should coincide with Coulomb shears (surfaces upon which the Coulomb failure criterion obtains). (In fact, this need not be the case; see de Joselin de Jong [1971, p. 163].) To the extent that this assumption is true, the orientation of the R_1 shears should define the orientation of the axis of principal compression, but even then there are problems in interpreting the observed orientations of the R_1 shears. For example, it is not known at what shear strain those prominent shears developed nor to what extent they have been rotated in subsequent deformation. Moreover, the observed shears show a range of inclinations to the plane of the saw cut, from an inclination of near zero at the gouge rock interface to 20° or more in the interior of the layer. Presumably, deforma-

tion is not homogeneous across the layer but rather is concentrated in shear bands within the layer. Thus we do not know which segment of the R_1 shear is relevant to the deformation being observed. Finally, the range of inclinations of the R_1 shears predicted for Coulomb plasticity for different saw cut angles is not large. The predicted inclination of the R_1 shears to the plane of the saw cut is $\xi - \pi/4 + (\tan^{-1} \mu_i)/2$, which for $\mu_i = 0.8$ is $\xi - 25.67^\circ$. As shown in Table 2, that inclination tends to increase with saw cut angle, but the increase is not large. Although we did not observe such a systematic increase with saw cut angle in the gouge layers, the observed inclinations of the shears ranged from near 0° to $>20^\circ$ for each saw cut angle. Thus the range of observations for an individual saw cut exceeded the range of the systematic effect expected. Our observations on the inclination of the R_1 shears at particular saw cut angles (inclination of $15^\circ \pm 5^\circ$ independent of saw cut angle) are consistent with those of other investigators (Table 2). Proper experiments to describe the origin of the structural fabrics observed in fault model gouge layers have been reported by Logan *et al.* [1992] and Gu and Wong [1994].

Intense shears were observed to develop along the gouge-rock interface in the saw cuts for 30° [Byerlee *et al.*, 1978], 35° [Logan *et al.*, 1979], and 45° [Marone *et al.*, 1990] saw cuts. Indeed, Logan *et al.* [1979, pp. 307, 312, and 314] found that slip across the 35° saw cuts was principally accommodated by such boundary shears (shears close to the edge of the saw cut but within the gouge). If this were the principal mode of accommodation for all saw cut angles, then the strength of all saw cuts should be $\tau_f = \mu_i \sigma_f$. That is, one strength line (Figure 4b) should represent all saw cut angles, and the locus of the observed apparent coefficients of friction μ_a in Figure 6a should be a vertical line (μ_a independent of α). That is clearly not the case.

Failure of the saw cuts in these triaxial experiments furnishes examples of noncoaxiality, the divergence between the orientations of the principal axes of stress

and incremental strain [Mandl, 1988, pp. 312–313]. Although shear deformation of the sand layer within the saw cut is apparently accommodated by cooperative slip on pairs of Coulomb shears, the net deformation across the sand layer is simple shear parallel to the saw cut (i.e., apparent slip on the saw cut). The principal contraction axis within the gouge then makes an angle of 45° with the plane of the saw cut. The principal compression axis within the gouge makes an angle ξ with the plane of the saw cut. Values of ξ calculated from the observed τ_f/σ_f ratio and $\mu_i = 0.8$ through equation (2) for each saw cut angle are shown in Table 1. Only for saw cut angles 45° and 50° is ξ close to 45° , the inclination of the principal contraction axis.

Conclusions

After the initial stages of compaction of the gouge layer in the fault model (i.e., for shear strain >1), changes in the apparent friction across the model fault are explained by the rotation of the principal stress axes within the gouge layer. To the extent that deformation within the gouge layer is explained by Coulomb plasticity, the orientation (Figure 7) of the principal compression axis within the gouge layer in a triaxial test can be followed given only the coefficient of internal friction of the gouge and the usual stress measurements (σ'_1 and P_c). Our experiments indicate that in triaxial tests the principal compression axis in the gouge rotates so as to become parallel to the cylinder axis (Figure 8a). In the limiting state (principal compression axis parallel to cylinder axis) the stress state in the gouge would become the same as the stress state in the granite cylinder, and failure of the gouge layer would be independent of the saw cut angle. However, that state was only approached in our experiments.

Appendix: Orientation of Principal Compression Axis

The Mohr circle that describes the stress state in the gouge layer at failure is defined by the observed stresses σ_f and τ_f (equation (1)) across the plane of the saw cut and the premise that the Mohr circle must be tangent to the Coulomb failure envelope. Here we assume that the failure envelope is a straight line with zero intercept and slope $\mu_i = \tan \phi$. The family of Mohr circles tangent to that envelope is described by (Figure 5b)

$$(\sigma - \sigma_m)^2 + \tau^2 = \sigma_m^2 \tan^2 \chi = \sigma_m^2 \sin^2 \phi \quad (A1)$$

where $\sigma_m = (\sigma_1 + \sigma_2)/2$ [Mandl, 1988, pp. 300–301]; σ_1 and σ_2 are, of course, the principal stresses within the gouge. The value of σ_m is defined by the requirement that (A1) must be satisfied for $\sigma = \sigma_f$ and $\tau = \tau_f$. Substituting those values for σ and τ in (A1) and solving for σ_m , one finds

$$\sigma_m/\sigma_f = [1 \pm (\sin^2 \phi - (\tau_f/\sigma_f)^2 \cos^2 \phi)^{1/2}] / \cos^2 \phi \quad (A2)$$

Table 2. Comparison of Predicted ($\mu_i = 0.8$) and Observed Inclinations (in degrees) of R_1 Shears to Plane of the Saw Cut

α , deg	$\xi - 25.67^\circ$, deg	Observed Inclination, deg
20	6.6	
25	2.6	
30	8.4	$10^a, 20^b$
35	10.2	15^c
40	12.4	
45	16.5	$15^d, 20^b$
50	20.0	

^a Gu and Wong [1994].

^b Byerlee *et al.* [1978].

^c Logan *et al.* [1979].

^d Marone *et al.* [1990].

The Mohr circle tangent to the failure envelope and passing through (σ_f, τ_f) is then given by (A1) with σ_m given by (A2).

We can now solve for the angle ξ between the principal compression axis σ_1 within the gouge and the saw cut. The angle γ , the complement of ξ , is defined by the usual Mohr construction (Figure 5b): 2γ is the angle subtended from $(\sigma_m, 0)$ by the points (σ_f, τ_f) and $(\sigma_1, 0)$. From Figure 5b,

$$\tan(2\gamma) = \tau_f / (\sigma_f - \sigma_m) \quad (\text{A3})$$

and

$$\xi = \pi/2 - \gamma = \pi/2 - 0.5 \tan^{-1} \left[\frac{\tau_f / \sigma_f}{(1 - \sigma_m / \sigma_f)} \right] \quad (\text{A4})$$

Using (A2) and $\mu_i = \tan \phi$, one may write this relation in the form of equation (2). That relation, in a slightly different form, was given earlier by Gu and Wong [1994, p. 417].

For the particular case in which $\xi = \alpha$, the saw cut angle, (A4) implies

$$\sigma_m / \sigma_f = 1 + (\tau_f / \sigma_f) / \tan 2\alpha$$

Equation (1) implies that

$$(\sigma'_1 + P_c) / (2\sigma_f) = 1 + (\tau_f / \sigma_f) / \tan 2\alpha$$

Therefore at failure, $\sigma_m = (\sigma'_1 + P_c) / 2$, and the Mohr circle representing the stress state in the gouge layer is concentric with the Mohr circle representing the stress state in the granite cylinder. Moreover, because the two Mohr circles have a common point (σ_f, τ_f) , the Mohr circles are then identical, and the stress state in the gouge layer is the same as that in the granite cylinder.

Acknowledgments. We thank Robert Summers for performing these experiments. His careful work resulted in the excellent level of repeatability that made possible the analysis presented here.

References

- Byerlee, J. D., The frictional characteristics of Westerly granite, Ph.D. thesis, 179 pp., Mass. Inst. of Technol., Cambridge, June 1966.
- Byerlee, J. D., and J. C. Savage, Coulomb plasticity within the fault zone, *Geophys. Res. Lett.*, **19**, 2341–2344, 1992.

- Byerlee, J., V. Mjachkin, R. Summers, and O. Voevoda, Structures developed in fault gouge during stable sliding and stick-slip, *Tectonophysics*, **44**, 161–171, 1978.
- de Josselin de Jong, G., The double sliding, free rotating model for granular assemblies, *Geotechnique*, **21**, 155–163, 1971.
- Gu, Y., and T.-F. Wong, Development of shear localization in simulated gouge: Effect of cumulative slip and gouge particle size, *Pure Appl. Geophys.*, **143**, 389–423, 1994.
- Hansen, B., Shear box tests on sand, *Proc. Int. Conf. Soil Mech. Found. Eng.* **5th**, **1**, 127–131, 1961.
- Jaeger, J. C., and N. G. W. Cook, *Fundamentals of Rock Mechanics*, Chapman and Hall, New York, 1971.
- Logan, J. M., M. Friedman, N. Higgs, C. Dengo, and T. Shimamoto, Experimental studies of simulated gouge and their applications to studies of natural fault zones, in *Proceedings of Conference VIII: Analysis of Actual Fault Zones in Bedrock*, U.S. Geol. Surv. Open File Rep. 79–1299, 305–343, 1979.
- Logan, J. M., C. A. Dengo, N. G. Higgs, and Z. Z. Wang, Fabrics of experimental fault zones: Their development and relationship to mechanical behavior, in *Fault Mechanics and Transport Properties of Rocks*, edited by B. Evans and T.-F. Wong, pp. 33–67, Academic, San Diego, Calif., 1992.
- Mandl, G., *Mechanics of Tectonic Faulting*, Elsevier, New York, 1988.
- Marone, C., C. B. Raleigh, and C. H. Scholz, Frictional behavior and constitutive modeling of simulated fault gouge, *J. Geophys. Res.* **95**, 7007–7025, 1990.
- Rice, J. R., Fault stress state, pore pressure distributions, and the weakness of the San Andreas fault, in *Fault Mechanics and Transport Properties in Rocks*, edited by B. Evans and T.-F. Wong, pp. 475–503, Academic, San Diego, Calif., 1992.
- Scott, D. R., D. A. Lockner, J. D. Byerlee, and C. G. Sammis, Triaxial testing of Lopez fault gouge at 150 MPa mean effective stress, *Pure Appl. Geophysics*, **142**, 749–775, 1994a.
- Scott, D. R., C. J. Marone, and C. G. Sammis, The apparent friction of granular fault gouge in sheared layers, *J. Geophys. Res.*, **99**, 7231–7246, 1994b.
- Summers, R., and J. Byerlee, Summary of results of frictional sliding studies at confining pressures up to 6.98 kb, in selected rock materials, U.S. Geol. Surv. Open File Rep. 77–142, 1–129, 1977.
- Zoback, M. D., and J. D. Byerlee, Effect of high-pressure deformation on the permeability of Ottawa sand, *AAPG Bull.*, **60**, 1531–1542, 1976.

J. D. Byerlee, D. A. Lockner, and J. C. Savage, U.S. Geological Survey, MS/977, 345 Middlefield Road, Menlo Park, CA 94025. (e-mail: jsavage@isdmnl.wr.usgs.gov)

(Received February 7, 1996; revised June 21, 1996; accepted June 25, 1996.)